

# Scale-Equivariant Imaging: Self-Supervised Learning for Image Super-Resolution and Deblurring

Jérémy Scanvic , Mike Davies , Patrice Abry , Julián Tachella 

**Abstract**—Self-supervised methods have recently proved to be nearly as effective as supervised ones in various imaging inverse problems, paving the way for learning-based approaches in scientific and medical imaging applications where ground truth data is hard or expensive to obtain. These methods critically rely on invariance to translations and/or rotations of the image distribution to learn from incomplete measurement data alone. However, existing approaches fail to obtain competitive performances in the problems of image super-resolution and deblurring, which play a key role in most imaging systems. In this work, we show that invariance to roto-translations is insufficient to learn from measurements that only contain low-frequency information. Instead, we propose scale-equivariant imaging, a new self-supervised approach that leverages the fact that many image distributions are approximately scale-invariant, enabling the recovery of high-frequency information lost in the measurement process. We demonstrate throughout a series of experiments on real datasets that the proposed method outperforms other self-supervised approaches, and obtains performances on par with fully supervised learning.

## I. INTRODUCTION

Inverse problems are ubiquitous in scientific imaging and medical imaging. Linear inverse problems are generally modelled by the forward process

$$y = A(z) + \varepsilon, \quad (1)$$

where  $y$  represents the observed measurements,  $z$  represents the latent image,  $A$  is the imaging operator, and  $\varepsilon$  depicts the noise corrupting the measurements. In this paper, we focus on additive white Gaussian noise but our results can easily be generalized for other noise distributions, e.g., Poisson, or mixed Gaussian-Poisson. Recovering  $z$  from the noisy measurements is generally ill-posed, as the forward operator is often rank-deficient, e.g., when the number of measurements is smaller than the number of image pixels. Moreover, even when the forward operator is not rank-deficient, it might still be ill-conditioned, and reconstructions might be very sensible to noise (for example, in image deblurring problems).

There is a wide range of approaches for solving the inverse problem, i.e., recovering  $z$  from  $y$ . Classical methods rely on hand-crafted priors, e.g., a total variation, together with optimization algorithms to obtain a reconstruction that agrees with the observed measurements and the chosen prior [1], [2]. These model-based approaches often obtain suboptimal results due to a mismatch between the true image distribution and the hand-crafted priors. An alternative approach leverages a

dataset of reference images and associated measurements in order to train a reconstruction model [3]. While this approach generally obtains state-of-the-art performance, it is often hard to apply it to problems where ground truth images are expensive or even impossible to obtain.

In recent years, self-supervised methods have highlighted the possibility of learning from measurement data alone, thus bypassing the need for ground truth references. These methods focus either on taking care of noisy data and/or a rank-deficient operator. Noise can be handled through the use of Stein’s unbiased risk estimator if the noise distribution is known [4], or via Noise2x techniques [5]–[7] which require milder assumptions on the noise distribution such as independence across pixels [7]. Rank-deficient operators can be handled using measurement data associated with multiple measurement operators  $A_1, \dots, A_G$  (each with a different nullspace) [8], [9], or by assuming that the image distribution is invariant to certain groups of transformations such as translations or rotations [10], [11].

Self-supervised image deblurring methods have been proposed in settings where the images are blurred with multiple kernels [12], however this assumption is not verified in many applications. Moreover, self-supervised methods that rely on a single operator (e.g., a single blur kernel) [10], [11], have not been applied to inverse problems with a single forward operator that removes high-frequency information such as image super-resolution and image deblurring, except for methods exploiting internal/external patch recurrence [13] which assume noiseless measurements, thus not being easily generalizable to other inverse problems.

Image deblurring and super-resolution are two inverse problems particularly difficult to solve using self-supervised methods. The former is severely ill-conditioned, and the latter is rank-deficient. This makes methods that minimize the measurement consistency error inapplicable as they cannot retrieve any information that lies within the nullspace [10] or where the forward operator is ill-conditioned, whenever there is even the slightest amount of noise present.

In this work, we propose a new self-supervised loss for training reconstruction networks for super-resolution and image deblurring problems which relies on the assumption that the underlying image distribution is scale-invariant, and can be easily applied to any linear inverse problem, as long as the forward process is known. Figure 1 shows an overview of that loss. The main contributions are the following:

- 1) We introduce a new theoretical framework proving that scaling transforms play a key role in learning from bandlimited images which includes the important problems of deblurring and super-resolution.

Jérémy Scanvic, Patrice Abry and Julián Tachella are with ENSL, CNRS, Laboratoire de Physique, F-69364 Lyon, France.

Mike Davies is with the School of Engineering, University of Edinburgh, Edinburgh, EH9 3FB, UK.

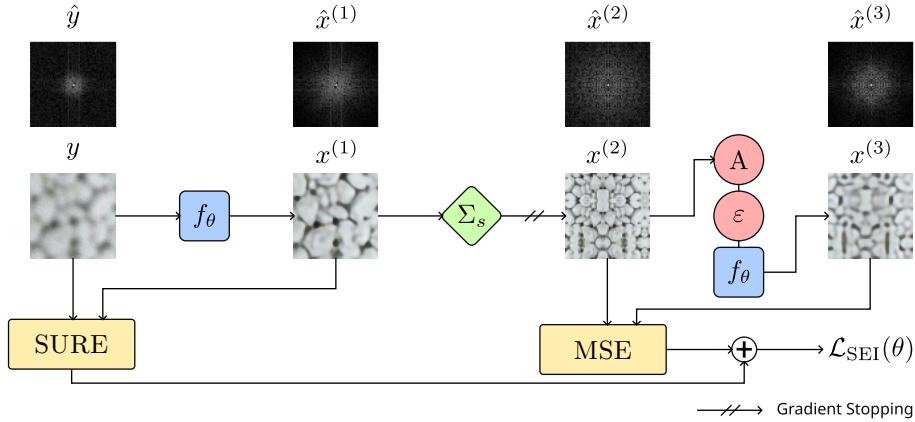


Fig. 1. **Scale-equivariant imaging.** The proposed loss is the sum of the SURE loss  $\mathcal{L}_{\text{SURE}}(\theta)$  which penalizes reconstruction error in the measurement domain, and of the scale-equivariant loss  $\mathcal{L}_{\text{SEQ}}(\theta)$  by viewing  $x^{(1)} = f_{\theta}(y)$  as a ground truth which might lack high-frequency content, and the downsampled image  $x^{(2)}$  as another one which has high-frequency content, and finally by penalizing the mean squared error of the reconstruction  $x^{(3)}$  obtained from a noisy measurement of  $x^{(2)}$ . The difference in high-frequency content is shown by  $\hat{x}^{(1)}$  and  $\hat{x}^{(2)}$ , the discrete Fourier transforms of  $x^{(1)}$  and  $x^{(2)}$ . One of our key contributions is stopping the gradient of  $x^{(2)}$  during the stochastic gradient descent.

- 2) We propose a new self-supervised loss for image deblurring and super-resolution leveraging the scale-invariance of typical image distributions to recover high-frequency information directly from corrupted images.
- 3) We conduct a series of experiments on images from multiple image distributions corrupted using varying blur filters and downsampling operators, showing that scale-equivariant imaging (SEI) performs on par with fully-supervised models and outperforms other state-of-the-art self-supervised methods.

## II. RELATED WORK

*a) Supervised approaches:* Most state-of-the-art super-resolution and image deblurring methods rely on a dataset containing ground truth references [14]–[17]. However, in many scientific imaging problems such as fluorescence microscopy and astronomical imaging, having access to high-resolution images can be difficult, or even impossible [18].

*b) Prior-based approaches:* A family of super-resolution and image deblurring methods rely on plug-and-play priors [19] and optimization methods. Other approaches rely on the inductive bias of certain convolutional architectures, i.e., the deep image prior [20], [21]. Some methods combine both techniques [22]. However, these approaches can provide sub-optimal results if the prior is insufficiently adapted to the problem.

*c) Stein’s Unbiased Risk Estimate:* Stein’s unbiased risk estimate is a popular strategy for learning from noisy measurement data alone, which requires knowledge of the noise distribution and of the forward model [4], [23], [24]. However, for image super-resolution and image deblurring, the forward operator is typically either rank-deficient or at least severely ill-conditioned, and the SURE estimates can only capture discrepancies in the range of the forward operator.

*d) Noise2x:* The Noise2Noise method [6] shows that it is possible to learn a denoiser in a self-supervised fashion if two independent noisy realizations of the same image are available for training, without explicit knowledge of the noise

distribution. Related methods extend this idea to denoising problems where a single noise realization is available, e.g., Noise2Void [5] and Noise2Self [7], and to general linear inverse problems, e.g., Noise2Inverse [25]. However, all of these methods crucially require that the forward operator is invertible and well-conditioned, which is not the case for super-resolution and most deblurring problems.

*e) Equivariant imaging:* The equivariant imaging (EI) method leverages the invariance of typical image distributions to rotations and/or translations to learn from measurement data alone, in problems where the forward operator is incomplete such as sparse-angle tomography, image inpainting and magnetic resonance imaging [10], [11], [26]. However, this approach requires the forward operator to not be equivariant to the rotations or translations. The super-resolution problems and image deblurring problems with an isotropic blur kernel do not verify this condition, and existing EI methods cannot be used.

*f) Patch recurrence methods:* Internal patch recurrence of natural images can be exploited to learn to super-resolve images without high-resolution references [13]. However, while this self-supervised learning method can be extended to collections of low-resolution images via external patch recurrence, it cannot be easily generalized to more general inverse problems (e.g., image deblurring) and noisy measurement data. The method proposed in this work generalizes the idea of patch recurrence to scale-invariance and can be applied to any imaging inverse problem where high-frequency information is missing.

## III. LEARNING FROM BANDLIMITED IMAGES

Imaging inverse problems are solved by finding a reconstruction function  $f : y \mapsto z$  that maps the observed measurements  $y \in \mathcal{Y}$  to the corresponding latent images  $z \in \mathcal{Z}$ . Self-supervised algorithms attempt to learn this function from a dataset of measurements  $\{y_1, \dots, y_N\} \subset \mathcal{Y}$  which raises the question of whether it is theoretically possible in the

first place. The analysis is typically broken down in two subproblems [27]:

- **Model identification.** Is the set of latent images  $\mathcal{Z}$  fully determined by the set of measurements  $\mathcal{Y}$ ?
- **Image recovery.** If the set of images  $\mathcal{Z}$  is fully identified, is there a reconstruction function  $f : y \mapsto z$  mapping measurements back to the corresponding latent image?

In this section, we focus on the problem of model identification for bandlimiting operators (e.g., blur filters and downsampling operators) and show that scale-invariant signal sets  $\mathcal{Z}$  are identifiable up to an arbitrary (fixed) frequency, unlike rotation-invariant ones. Unique image recovery given a known image set  $\mathcal{Z}$  is possible, under appropriate conditions, if the set is low-dimensional. This has been studied in the compressive sensing literature (albeit generally under the assumption of random forward operators) [28] but is also tacitly assumed in any image reconstruction process. We will similarly make this assumption here.

We consider images as functions  $z : \mathbb{R}^2 \rightarrow \mathbb{C}^d$  where  $d \geq 1$  denotes the number of channels. Formally, we model the set of images as a subset  $\mathcal{Z}$  of the Schwartz space<sup>1</sup>  $\mathcal{S}$  of functions mapping  $\mathbb{R}^2$  to  $\mathbb{C}^d$ . The problems of super-resolution and deblurring fall under the umbrella of image recovery from bandlimited measurements. Thus in this section, to simplify notation we assume that the forward operator is modelled as  $y = h * z$ , where  $h \in \mathcal{S}$  is a filter acting on images  $z$  by convolution. Moreover, we assume that  $h$  has a finite bandwidth  $0 \leq \xi_h < \infty$ , defined as:

**Definition 1** (Bandlimited, bandwidth). *Let  $\varphi \in \mathcal{S}$ , we say that  $\varphi$  is bandlimited if for some  $\xi_\varphi \geq 0$ ,*

$$\hat{\varphi}(\xi) = 0, \forall \xi \in \mathbb{R}^2, \|\xi\|_2 \geq \xi_\varphi, \quad (2)$$

where  $\hat{\varphi}(\xi) = \int_{\mathbb{R}^2} \varphi(u) e^{-i2\pi\xi^\top u} du$  is the Fourier transform of  $\varphi$ . In that case, we call the smallest such  $\xi_\varphi$  the bandwidth of  $\varphi$ .

While physical images  $z$  are typically not bandlimited, the measurements  $y = h * z$  have bandwidth at most  $\xi_h$ , and due to the Shannon-Nyquist's sampling theorem, they can be represented by discrete samples on a regular grid of sampling rate  $2\xi_h$  [29].

In the self-supervised learning setting, we only observe the set of bandlimited measurements

$$\mathcal{Y} = \{h * z, z \in \mathcal{Z}\}. \quad (3)$$

and the key question is whether we can recover the set of images  $\mathcal{Z}$  from the set of measurements  $\mathcal{Y}$ . This formulation has been studied when  $\mathcal{Z}$  is a subset of the finite-dimensional space  $\mathbb{R}^n$  under the assumption that ground truth images have finite bandwidth [9]. Here, we consider the more general setting where  $\mathcal{Z}$  contains continuous images that can have an infinite bandwidth. According to Shannon-Nyquist's sampling theorem [29], it is impossible to represent them faithfully on a (finite) grid of pixels, no matter how fine it is. This makes

<sup>1</sup>The Schwartz space  $\mathcal{S}$  is dense in  $L^2$ , and unlike  $L^2$  it is closed under convolution, making it a very general model for studying bandlimited inverse problems.

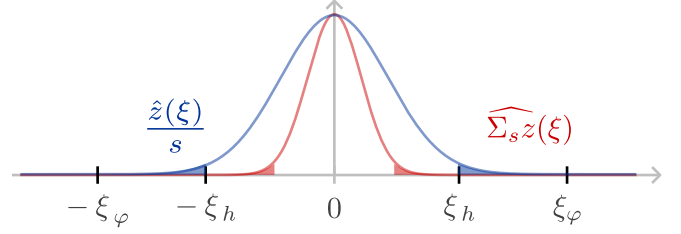


Fig. 2. **Spectral effect of rescaling.** In bandlimited problems such as image super-resolution and deblurring, the image frequencies are only observed on a low-frequency band  $[0, \xi_h)$  determined by the bandlimiting operator (e.g., blur and anti-aliasing filters), and the goal is to recover texture information in a higher frequency band  $(\xi_h, \xi_\varphi)$  where  $\xi_\varphi/\xi_h$  can be interpreted as the increase in effective resolution. Scale-invariance makes this possible as the spectral information is available at all scales: an image  $z(u)$  and the rescaled image  $\Sigma_s z(u)$  with scaling factor  $s$  have the same spectral content except in different frequency bands.

the formulation of the problem impractical to work with and instead we propose to recover the set

$$\mathcal{X} = \{\varphi * z, z \in \mathcal{Z}\}, \quad (4)$$

which contains low-pass filtered versions  $x = \varphi * z$  of the images in  $\mathcal{Z}$ , using a bandlimiting filter  $\varphi \in \mathcal{S}$  with the desired increased bandwidth  $\xi_\varphi > \xi_h$ . In this way, the images in  $\mathcal{X}$  can be represented in a discrete grid with sampling rate  $2\xi_\varphi$ . In the context of image deblurring,  $\xi_h$  represents the resolution of the blurry images and  $\xi_\varphi$  the target resolution, and for image super-resolution the ratio  $\xi_\varphi/\xi_h$  can be interpreted as the upsampling rate.

In general, the set  $\mathcal{X}$  cannot be entirely known from the observation set  $\mathcal{Y}$  as it only contains information about the lower-frequency content of the latent images  $z \in \mathcal{Z}$ , and none for the frequencies in  $\xi_h < \xi \leq \xi_\varphi$ . However, if  $\mathcal{Z}$  is known to be invariant to a group action  $T_g : \mathcal{S} \mapsto \mathcal{S}$ , with  $g \in G$  then the set of observed images is equal to the augmented set of observed images [9]

$$\mathcal{Y}_G = \{h * T_g z, z \in \mathcal{Z}, g \in G\}. \quad (5)$$

In this case, depending on the specific group action,  $\mathcal{Y}_G$  might have the entirety of the information of  $\mathcal{Z}$  up to the higher frequency  $\xi_\varphi > \xi_h$ . This amounts to saying that the set  $\mathcal{X}$  can be recovered from the set  $\mathcal{Y}_G$ . The three most common invariances to group actions of natural image distributions are rotations, translations and scaling transforms which are defined as follows:

**Definition 2** (Scaling transforms, translations and rotations). *Let  $z \in \mathcal{S}$ . We define the action by the groups of scaling transforms  $\Sigma$ , translations  $\tau$  and rotations  $R$  by*

$$(\Sigma_s z)(u) = z(s^{-1}u), \quad u \in \mathbb{R}^2, s \in (0, \infty), \quad (6)$$

$$(\tau_v z)(u) = z(u - v), \quad u \in \mathbb{R}^2, v \in \mathbb{R}^2, \quad (7)$$

$$(R_\theta z)(u) = z(P_\theta^{-1} u), \quad u \in \mathbb{R}^2, \theta \in [0, 2\pi), \quad (8)$$

where  $P_\theta \in \mathbb{R}^{2 \times 2}$  is the rotation matrix for angle  $\theta$ .

The choice of the group  $G$  plays a fundamental role in the recovery of the information lost in the measurement process. While most previous works have focused on rotations and

translations [9]–[11], here we show that these are not sufficient for learning from bandlimited measurements alone:

**Theorem 1.** *Let  $h, \varphi \in \mathcal{S}$ . If  $h$  and  $\varphi$  are bandlimited with bandwidths  $\xi_h < \xi_\varphi$ , then there are sets  $\mathcal{Z}_1, \mathcal{Z}_2 \subseteq \mathcal{S}$  such that*

- $\mathcal{Z}_1$  and  $\mathcal{Z}_2$  are roto-translation invariant, that is

$$\tau_v R_\theta z \in \mathcal{Z}_\ell, \quad z \in \mathcal{Z}_\ell, v \in \mathbb{R}^2, \theta \in [0, 2\pi), \ell \in \{1, 2\}, \quad (9)$$

- for  $\mathcal{Y}_1 = h * \mathcal{Z}_1$  and  $\mathcal{Y}_2 = h * \mathcal{Z}_2$  as in Eq. (3),

$$\mathcal{Y}_1 = \mathcal{Y}_2 \quad (10)$$

- for  $\mathcal{X}_1 = \varphi * \mathcal{Z}_1$  and  $\mathcal{X}_2 = \varphi * \mathcal{Z}_2$  as in Eq. (4),

$$\mathcal{X}_1 \neq \mathcal{X}_2. \quad (11)$$

For the sake of brevity, we only exhibit one example of such sets  $\mathcal{Z}_1$  and  $\mathcal{Z}_2$  in the proof (in the appendix) but it is possible to find a matching  $\mathcal{Z}_2$  for any candidate  $\mathcal{Z}_1$  by altering it in the frequency band  $(\xi_h, \xi_\varphi)$ .

Intuitively the action by rotations and translations does not increase the bandwidth of an image and thus does not provide information in the frequency range  $\xi_h < \xi < \xi_\varphi$ . On the contrary, the action by scaling modifies the bandwidth of an image (illustrated in Figures 1 and 2), which allows us to identify the set  $\mathcal{X}$  from the bandlimited images alone.

**Theorem 2.** *Let  $h, \varphi \in \mathcal{S}$  and  $\mathcal{Z} \subseteq \mathcal{S}$ . If  $\mathcal{Z}$  is scale-invariant, that is*

$$\Sigma_s z \in \mathcal{Z}, \forall z \in \mathcal{Z}, s \in (0, \infty), \quad (12)$$

$\varphi$  is bandlimited, and  $\hat{h}(0) \neq 0$ , where  $\hat{h}$  is the Fourier transform of  $h$ , then the set  $\mathcal{X}$  defined in Eq. (4) is uniquely determined by the set of observed images  $\mathcal{Y}$  defined in Eq. (3). More precisely, there is a  $s \geq \frac{\xi_\varphi}{\xi_h}$  which only depends on  $\varphi$  and  $h$ , for which  $\hat{h}(s^{-1}\xi) \neq 0$  as long as  $\|\xi\|_2 < \xi_\varphi$ , and

$$\mathcal{X} = \{x_y, y \in \mathcal{Y}\}, \quad (13)$$

where  $x_y \in \mathcal{S}$  is defined by

$$\hat{x}_y(\xi) = \begin{cases} \frac{\hat{\varphi}(\xi)\hat{y}(s^{-1}\xi)}{s\hat{h}(s^{-1}\xi)}, & \text{if } \|\xi\|_2 < \xi_\varphi, \\ 0, & \text{otherwise.} \end{cases} \quad (14)$$

See the appendix for the detailed proofs. These results show that leveraging scale-invariance is crucial for learning from bandlimited measurements alone, and in the next section we present a practical self-supervised loss that exploits this property.

#### IV. PROPOSED METHOD

In this section, we assume that there is an approximately one-to-one correspondence between the latent images and the measured images which guarantees that image recovery is possible, and we expose our proposed method for deblurring and super-resolution that exploits the scale-invariance of typical image distributions.

As shown by Theorem 2, as long as the set of latent images is invariant to scale, there is enough information in the set of bandlimited images to uniquely determine the set of

images with an arbitrarily high bandwidth. This hints that self-supervised learning can be as effective as supervised learning for solving bandlimiting imaging problems like image super-resolution and deblurring.

In the problems of deblurring and super-resolution, the goal is to recover a high-resolution image  $x \in \mathbb{R}^n$  from a low-resolution image  $y \in \mathbb{R}^m$ . For notational simplicity, we represent images as vectors where every dimension corresponds to a different pixel but the method is designed to be used to learn a nonlinear reconstruction filter that takes in images of arbitrary size, e.g., a convolutional neural network (CNN) or a suitable vision transformer (ViT). The relation between  $x$  and  $y$  is modelled as

$$y = (h * x) \downarrow_r + \varepsilon \quad (15)$$

where  $\downarrow_r$  is the subsampling operator by factor  $r$ , and  $\varepsilon \sim \mathcal{N}(0, \sigma^2 I)$  is additive Gaussian noise<sup>2</sup>. In super-resolution problems  $h$  is the anti-aliasing filter and  $r > 1$  whereas in deblurring problems  $h$  is the blur kernel and  $r = 1$ . Self-supervised learning-based methods attempt to solve this problem by learning a reconstruction function<sup>3</sup>  $f_\theta : y \mapsto x$  parametrized by a neural network with learnable weights  $\theta \in \mathbb{R}^p$  using a dataset of blurry/low-resolution images only  $\{y_i\}_{i=1}^N$ .

a) *Stein's unbiased risk estimator:* The SURE loss [4], [11] is a self-supervised loss that serves as an unbiased estimator of the mean squared error (MSE) in measurement space

$$\mathbb{E}_{x,y} \|(h * f_\theta(y)) \downarrow_r - (h * x) \downarrow_r\|_2^2, \quad (16)$$

which does not require access to ground truth images  $x$ . The SURE loss for measurements corrupted by Gaussian noise of standard deviation  $\sigma$  [11] is given by:

$$\mathcal{L}_{\text{SURE}}(\theta) = \sum_{i=1}^N \frac{1}{m} \|(h * f_\theta(y_i)) \downarrow_r - y_i\|_2^2 - \sigma^2 + \frac{2\sigma^2}{m} \text{div}[(h * f_\theta) \downarrow_r](y_i). \quad (17)$$

where the divergence  $\text{div}$  is approximated using a Monte-Carlo estimate [30]. It is worth noting that, in the noiseless setting, i.e.,  $\sigma = 0$ , the SURE loss is equal to a measurement consistency constraint  $(h * f_\theta(y)) \downarrow_r = y$ ,

$$\mathcal{L}_{\text{MC}}(\theta) = \sum_{i=1}^N \frac{1}{m} \|(h * f_\theta(y_i)) \downarrow_r - y_i\|_2^2. \quad (18)$$

which does not penalize the reconstructions in the nullspace of  $A$ . In the setting of super-resolution and image deblurring, the nullspace of the operator is associated with the high-frequencies of the image  $x$ , and thus training with the SURE loss alone fails to reconstruct the high-frequency content.

We propose to minimize the training loss

$$\mathcal{L}_{\text{SEI}}(\theta) = \mathcal{L}_{\text{SURE}}(\theta) + \alpha \mathcal{L}_{\text{SEQ}}(\theta), \quad (19)$$

<sup>2</sup>We focus on Gaussian noise in this work and use the corresponding risk estimator – it is meant to be substituted for other noise distributions.

<sup>3</sup>For the problem to be well-defined, it is necessary that there is one-to-oneness between the large-bandwidth images and the small-bandwidth images.

TABLE I  
DEBLURRING AND SUPER-RESOLUTION PERFORMANCE. (BOLD) BEST PERFORMING METHOD, (BLUE) SECOND BEST.

Method	Gaussian filter (small)			Gaussian filter (medium)			Gaussian filter (large)			Box filter (small)			Box filter (medium)			Box filter (large)		
	PSNR	SSIM	LPIPS	PSNR	SSIM	LPIPS	PSNR	SSIM	LPIPS	PSNR	SSIM	LPIPS	PSNR	SSIM	LPIPS	PSNR	SSIM	LPIPS
Supervised	<b>30.7</b>	<b>0.923</b>	<b>0.064</b>	<b>25.9</b>	<b>0.803</b>	<b>0.249</b>	<b>23.7</b>	<b>0.694</b>	<b>0.361</b>	<b>29.1</b>	<b>0.879</b>	<b>0.107</b>	<b>27.3</b>	<b>0.825</b>	<b>0.171</b>	<b>25.4</b>	<b>0.755</b>	<b>0.255</b>
SEI (Ours)	<b>30.3</b>	<b>0.917</b>	<b>0.062</b>	<b>25.9</b>	<b>0.795</b>	<b>0.254</b>	<b>23.7</b>	<b>0.687</b>	<b>0.379</b>	<b>28.8</b>	<b>0.874</b>	<b>0.112</b>	<b>27.0</b>	<b>0.818</b>	<b>0.178</b>	<b>25.0</b>	<b>0.739</b>	<b>0.309</b>
CSS	29.1	0.899	0.202	24.2	0.707	0.462	22.8	0.622	0.549	26.0	0.804	0.282	24.2	0.713	0.418	23.1	0.640	0.508
SURE	26.3	0.731	0.257	23.2	0.594	0.447	21.1	0.490	0.538	25.8	0.754	0.234	24.5	0.675	0.329	23.3	0.595	0.437
BM3D	29.5	0.881	0.184	25.4	0.757	0.380	23.5	0.649	0.506	27.1	0.809	0.270	25.5	0.743	0.356	24.6	0.700	0.420
DIP	27.3	0.825	0.177	24.4	0.691	0.350	22.8	0.579	0.452	24.1	0.675	0.378	23.1	0.598	0.433	22.3	0.538	0.481
EI	28.0	0.835	0.247	24.8	0.718	0.360	22.7	0.594	0.445	24.5	0.709	0.344	23.2	0.646	0.385	22.9	0.611	0.463
Blurry images	26.4	0.794	0.269	22.8	0.597	0.461	21.2	0.494	0.604	23.4	0.629	0.359	21.9	0.528	0.464	21.0	0.465	0.552

Method	Downsampling ( $\times 2$ )			Downsampling ( $\times 3$ )			Downsampling ( $\times 4$ )		
	PSNR $\uparrow$	SSIM $\uparrow$	LPIPS $\downarrow$	PSNR $\uparrow$	SSIM $\uparrow$	LPIPS $\downarrow$	PSNR $\uparrow$	SSIM $\uparrow$	LPIPS $\downarrow$
Supervised	<b>28.99</b>	<b>0.8821</b>	<b>0.1416</b>	<b>25.94</b>	<b>0.7833</b>	<b>0.2491</b>	<b>24.25</b>	<b>0.6983</b>	<b>0.3185</b>
SEI (Ours)	28.09	0.8500	0.1972	<b>25.29</b>	0.7436	0.3833	<b>23.73</b>	<b>0.6568</b>	0.4642
CSS	<b>28.50</b>	<b>0.8616</b>	<b>0.1781</b>	25.29	<b>0.7441</b>	0.3835	21.38	0.6126	0.5085
DIP	25.77	0.7673	0.2678	24.11	0.6828	<b>0.3649</b>	22.79	0.5915	<b>0.4447</b>
EI	27.76	0.8413	0.2469	25.13	0.7387	0.4108	23.51	0.6441	0.5132
Bicubic	27.23	0.8306	0.2986	24.67	0.7185	0.4660	23.26	0.6325	0.5882

where  $\alpha > 0$  is a trade-off parameter,  $\mathcal{L}_{\text{SURE}}(\theta)$  is given in Equation (17), and  $\mathcal{L}_{\text{SEQ}}(\theta)$  is the equivariant loss introduced below, which is inspired by the robust equivariant imaging loss [11]. In all experiments, we set  $\alpha = 1$ . The two contributions of our method are the use of the action by downscaling transforms instead of the action by shifts or by rotations, and stopping the gradient during the forward pass, as illustrated in Figure 1 (details are explained below).

In the forward pass, we first compute  $x_{i,\theta}^{(1)} = f_{\theta}(y_i)$ , which we view as an estimation of the  $i$ th ground truth image  $x_i$ . Next, we compute  $x_{i,\theta}^{(2)} = \Sigma_s x_{i,\theta}^{(1)}$ , where  $\Sigma_s$  is the downscaling transform by factor  $s \in (0, 1)$ , without propagating the gradient, which effectively leaves  $\nabla_{\theta} x_{i,\theta}^{(2)} = 0$ . Finally, we compute  $x_{i,\theta}^{(3)} = f_{\theta}(A x_{i,\theta}^{(2)} + \tilde{\varepsilon})$  where  $\tilde{\varepsilon}$  is sampled from  $\mathcal{N}(0, \sigma^2 I)$ . The three terms are used to compute  $\mathcal{L}_{\text{SURE}}$  and  $\mathcal{L}_{\text{SEQ}}$ , where  $\mathcal{L}_{\text{SEQ}}$  is defined as

$$\mathcal{L}_{\text{SEQ}}(\theta) = \sum_{i=1}^N \frac{1}{n} \|x_{i,\theta}^{(3)} - x_i^{(2)}\|_2^2. \quad (20)$$

*b) Downscaling transformations:* In all experiments,  $\Sigma_s$  consists in resampling the input image viewed as periodic on a (coarse) grid with a spacing of  $s^{-1}$  pixels, using bicubic interpolation. The grid center is chosen randomly at each call and the scale factor is chosen uniformly from  $\{.5, .75\}$ . Figure 3 shows two possible downscalings of an image patch.

*c) Gradient stopping:* The gradient-stopping step, which removes the dependence of  $x_{i,\theta}^{(2)}$  on the network weights  $\theta$  plays an important role in the self-supervised loss. Table II shows that gradient stopping significantly improves the performance of the self-supervised network for both image deblurring and image super-resolution, i.e., by about 1dB. Such gradient-stopping steps have proved crucial in various self-supervised representation learning methods and lead to significant performance increase [31], [32].

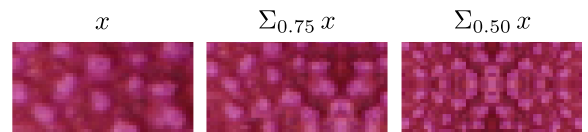


Fig. 3. **Implementation of the (down-)scaling transformations.** Scale-equivariant imaging (SEI) uses rescaled versions of network outputs as learning targets implemented as bicubic resampling on a coarser grid randomly sampled for each batch element. Using a coarser grid makes the resulting image close to the target manifold  $\mathcal{X}$  as its spectral information corresponds to the low-frequency content of the (unknown) target image thanks to the loss  $\mathcal{L}_{\text{SURE}}$  and to the scale-invariance of the latent image set  $\mathcal{Z}$ .

*d) Comparison to self-supervision via patch recurrence:* A related self-supervised approach to ours is the zero-shot super-resolution proposed by [13], which uses the measurements  $y_i$  as ground truth targets, and computes corresponding corrupted inputs applying the forward operator to  $y$ , i.e.,

$$\tilde{y} = (h * y) \downarrow_r + \tilde{\varepsilon} \quad (21)$$

where  $\tilde{\varepsilon}$  is sampled from a zero-mean Gaussian distribution with the same standard deviation. Then, a self-supervised loss is constructed as

$$\mathcal{L}_{\text{CSS}}(\theta) = \sum_{i=1}^N \frac{1}{m} \|y_i - f_{\theta}(\tilde{y}_i)\|_2^2 \quad (22)$$

which we name Classic Self-Supervised (CSS) loss. This approach is only valid when measurements  $y$  can be interpreted as images, such as in a super-resolution problem [13], however, it is unclear whether it is effective for solving general problems, e.g., compressed sensing.

The CSS method requires that the forward operator is a downsampling transformation and that the noise  $\varepsilon$  is sufficiently small, such that  $(h * y) \downarrow_r \approx x'$  for some  $x'$  which also belongs to the dataset. On the contrary, as the proposed method exploits scale-invariance on the reconstructed images, it can

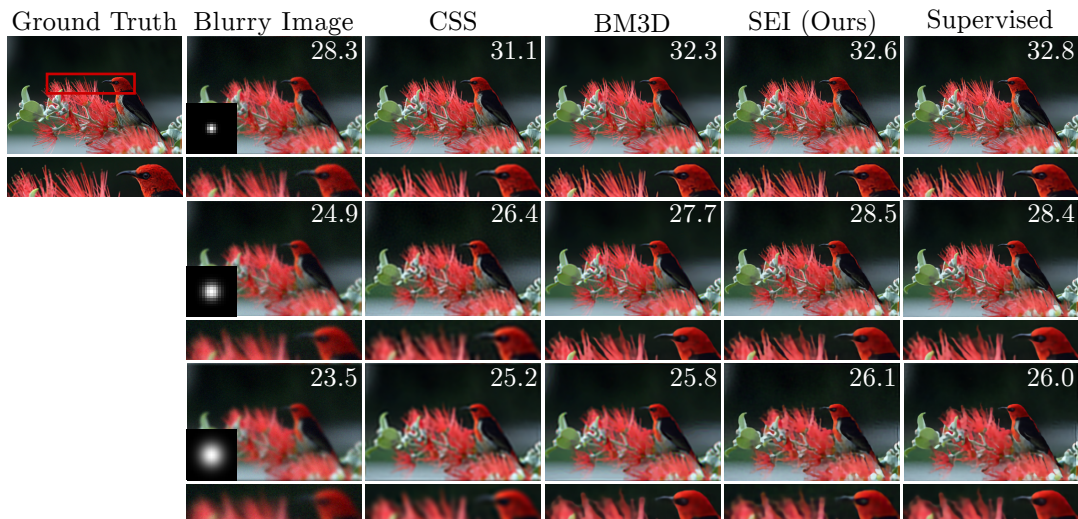


Fig. 4. **Visual comparison for Gaussian deblurring.** Top-right corner: PSNR, bottom-left corner: point-spread functions.

TABLE II  
ABLATION STUDY. GS: GRADIENT STOPPING.

	Gaussian filter (medium)			Box filter (medium)			Downsampling ( $\times 2$ )		
	PSNR	SSIM	LPIPS	PSNR	SSIM	LPIPS	PSNR	SSIM	LPIPS
✓	<b>25.9</b>	<b>0.795</b>	<b>0.254</b>	<b>27.0</b>	<b>0.818</b>	<b>0.178</b>	<b>28.1</b>	<b>0.850</b>	<b>0.197</b>
×	22.9	0.632	0.506	22.6	0.601	0.551	26.8	0.810	0.305

be used with any operator  $A$ . Thus, for the super-resolution problems with a small amount of noise, we expect to obtain a similar performance with both methods, whereas in the more challenging image deblurring problem we expect to observe a different performance across methods.

## V. EXPERIMENTS

We evaluate our method for non-blind deblurring and super-resolution on images corrupted by 1) Gaussian filters, 2) box filters, and 3) bicubic downsampling operators. This allows us to verify that our method performs well across different imaging modalities. We use SwinIR [17] as the architecture of our reconstruction network – one of the best-performing architectures for image super-resolution. In each setting, we provide a comparison with a wide variety of state-of-the-art methods, including the CSS method in Equation (22) [13], the diffusion method DiffPIR [33], (robust) equivariant imaging (EI) [11], GSURE [4], [34], the Plug-and-Play (PnP) method DPIR [35], BM3D [2] and Deep Image Prior (DIP) [20], [36]. For a fair comparison and to demonstrate the importance of the training loss in our method, we also compare against models trained the same way as ours except for the training loss. In addition to the self-supervised baselines, we compare with supervised baselines and show that our scale-equivariant imaging approach (SEI) compares favorably against them, even though it is fully self-supervised and does not have direct access to the underlying distribution of clean images. Our results show that our method performs better than other state-

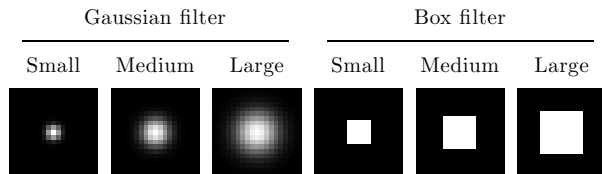


Fig. 5. **Point-spread functions.** Our method makes no assumption about the shape or strength of the blur kernel making it broadly applicable and in particular we verify that it performs well on Gaussian filters with standard deviation 1, 2 or 3 pixels, and for box filters with radius 2, 3 or 4 pixels.

of-the-art self-supervised methods and significantly improves the quality of corrupted images.

For every degradation model, we constitute pairs of clean and corrupted images that we use for training and evaluation. We evaluate all methods, using two dataset of natural images DIV2K [37] and Urban100 [38], and a dataset of computed tomography (CT) scans [39]. Figure 5 shows the 6 different blur kernels used for synthesizing some of the corrupted images, and the remaining ones are synthesized using bicubic downsampling with multiple sample rates (2 and 4). The resulting images are further corrupted by additive white Gaussian noise making the degradation model closer to real-world image degradations happening in most imaging systems. The standard deviation for the Gaussian noise is set to  $\sigma = 5/255$ . The 900 image pairs from DIV2K are split into 100 testing pairs and 800 training pairs, the 100 image pairs from Urban100 are split into 10 testing pairs and 90 testing pairs, and the 5092 pairs for CT scans are split into 100 testing pairs and 4992 training pairs. Tables I and IV show that scale-invariant imaging tends to perform as well as the supervised baseline and significantly better than the other state-of-the-art self-supervised methods, both across different imaging modalities and different image distributions. Examples of deblurred and upsampled images are shown in Figure 4.

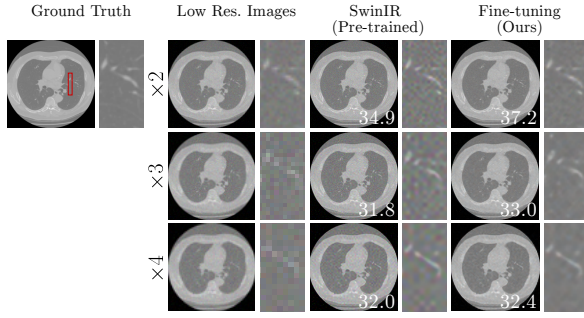


Fig. 6. **Fine-tuning on CT scans.** Self-supervised methods for super-resolution do not require ground truth images and can be used to fine-tune pre-trained models on test data directly. Here, we fine-tune models trained on natural images to upsample CT scans corrupted by additional Gaussian noise.

TABLE III  
FINE-TUNING PERFORMANCE. FT: FINE-TUNING.

FT	Downsampling ( $\times 2$ )			Downsampling ( $\times 3$ )			Downsampling ( $\times 4$ )		
	PSNR	SSIM	LPIPS	PSNR	SSIM	LPIPS	PSNR	SSIM	LPIPS
✓	<b>37.1</b>	<b>0.882</b>	<b>0.123</b>	<b>33.4</b>	<b>0.870</b>	<b>0.138</b>	<b>32.9</b>	<b>0.835</b>	<b>0.194</b>
×	34.9	0.804	0.260	32.0	0.799	0.370	32.4	0.816	0.398

a) *Fine-tuning*: Because it is fully self-supervised and unlike supervised methods, it is possible to use scale-equivariant imaging directly on test data. This enables fine-tuning models pre-trained on image distributions that might differ from the test data, generally resulting in better performing models. We evaluate this approach by fine-tuning 3 models on CT scans. The 3 models are pre-trained on pairs high and low-resolution images from DIV2K (natural images), each for a different sampling rate (2, 3, and 4), all with the same supervised training algorithm. The low-resolution images are synthesized using bicubic downsampling similarly to the low-resolution CT scans that we are using except for the absence of additional noise. Table III shows that the performance of the fine-tuned model is significantly greater than the performance of the pre-trained model, ranging from a .5 dB to a 2 dB difference in PSNR. Example of upsampled images are shown in Figure 6.

b) *Ablation studies*: In addition to the experiments comparing our method with various other methods, we also conduct an ablation study to evaluate the importance of gradient stopping, one of the key ingredients in scale-equivariant imaging. For each of the three degradation models, we train two models using our proposed method: one with and one without gradient stopping. Table II shows that gradient stopping improves the reconstructions by more than 2dB (PSNR) in all three cases. This is consistent with our broader empirical observation that gradient stopping consistently improves the performance of the proposed method.

#### A. Experimental details

a) *Performance metrics*: Similarly to [17], we convert reference images and image estimates from RGB to YCbCr, and we report the PSNR and the SSIM for the luminance (Y)

TABLE IV  
DEBLURRING PERFORMANCE ON ADDITIONAL DATASETS.

Method	Urban 100			CT scans		
	PSNR $\uparrow$	SSIM $\uparrow$	LPIPS $\downarrow$	PSNR $\uparrow$	SSIM $\uparrow$	LPIPS $\downarrow$
Supervised	<b>23.34</b>	<b>0.7271</b>	<b>0.1726</b>	<b>38.10</b>	<b>0.9502</b>	<b>0.0459</b>
SEI (Ours)	<b>23.63</b>	<b>0.7380</b>	<b>0.1689</b>	<b>34.05</b>	0.8828	<b>0.0908</b>
CSS	21.10	0.5827	0.4017	30.13	0.8747	0.2493
BM3D	23.16	0.6894	0.3170	33.81	<b>0.9216</b>	0.1850
DIP	20.34	0.4913	0.4450	30.19	0.7739	0.2922
Blurry images	18.99	0.3786	0.4468	27.79	0.7147	0.4250

channel. For LPIPS, the values are directly obtained from the RGB images as usual.

b) *Training hyperparameters*: We train all of the models using a batch size of 8, for 500 epochs for DIV2K, for 4000 epochs for Urban100, and for 100 epochs for the CT scans. For all trainings except fine-tuning ones, we use Adam [40] with an initial learning rate of 0.0005 for deblurring, and of 0.0002 for super-resolution, with  $\beta = (0.9, 0.999)$  in both cases. For fine-tuning, we use regular stochastic gradient descent (SGD) instead, with an initial learning rate of 0.01. This leads to more stable training dynamics and better resulting performance. Each model takes from 10 to 20 hours to train on a single recent GPU using SIDUS [41].

c) *Baselines hyperparameters*: For the supervised baseline (Supervised), we use the  $\ell^2$ -distance as the training loss. For deep image prior (DIP), we use a learning rate of 0.005 and random inputs of size  $16 \times 16$  with 32 channels. We use the network architecture proposed by [36], for at most 100 iterations and with early-stopping. For plug-and-play (PnP), we use the method proposed by [35]. The denoiser is pre-trained on images from various datasets [42], [43], including DIV2K.

## VI. CONCLUSION

In this work, we introduce scale-equivariant imaging (SEI), a new self-supervised method for image deblurring and super-resolution which recovers the missing high-frequency content in images corrupted by a blur filter or by a downsampling operator directly from the corrupted images and without using a single clean image. Throughout extensive experiments, we show that SEI can be as effective as fully-supervised methods and that it outperforms other state-of-the-art self-supervised methods, including diffusion and plug-and-play approaches. This is consistent both across different degradation models and across different image distributions, including natural and medical images.

Unlike previous works which focus on rotations and translations [10], [11], we show that the right symmetry to exploit for bandlimited imaging problems is the invariance to scaling transforms as it enables the recovery of high-frequency information lost in the imaging process. On the contrary, exploiting rotations and translations cannot help to recover any information beyond the bandwidth of the corrupted images. Moreover, we present a novel approach to model identification theory [9], which, instead of recovering the original set of

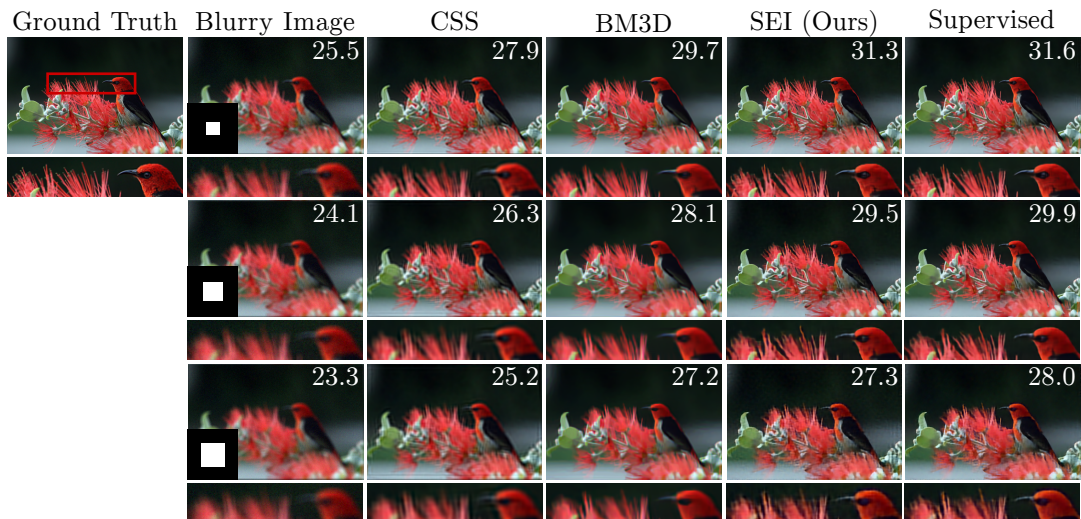


Fig. 7. **Visual comparison for box deblurring.** Bottom-left corner: point-spread function, top-right corner: PSNR.

latent images, focuses on the recovery of a projection of this set.

The promising results of SEI suggest that it could be applied to the significantly more difficult blind imaging problems where the degradation model is only partially known. We expect that exploiting the symmetries of the degradation model will prove crucial to solve these problems.

## REFERENCES

- [1] A. Chambolle and T. Pock, "An introduction to continuous optimization for imaging," *Acta Numerica*, vol. 25, pp. 161–319, 2016.
- [2] K. Dabov, A. Foi, V. Katkovnik, and K. Egiazarian, "Image denoising by sparse 3-d transform-domain collaborative filtering," *IEEE Transactions on image processing*, vol. 16, no. 8, pp. 2080–2095, 2007.
- [3] G. Ongie, A. Jalal, C. A. Metzler, R. G. Baraniuk, A. G. Dimakis, and R. Willett, "Deep learning techniques for inverse problems in imaging," *IEEE Journal on Selected Areas in Information Theory*, vol. 1, no. 1, pp. 39–56, 2020.
- [4] C. A. Metzler, A. Mousavi, R. Heckel, and R. G. Baraniuk, "Unsupervised Learning with Stein's Unbiased Risk Estimator," Jul. 2020, arXiv:1805.10531 [cs, stat]. [Online]. Available: <http://arxiv.org/abs/1805.10531>
- [5] A. Krull, T.-O. Buchholz, and F. Jug, "Noise2void-learning denoising from single noisy images," in *Proceedings of the IEEE/CVF conference on computer vision and pattern recognition*, 2019, pp. 2129–2137.
- [6] J. Lehtinen, J. Munkberg, J. Hasselgren, S. Laine, T. Karras, M. Aittala, and T. Aila, "Noise2Noise: Learning Image Restoration without Clean Data," in *Proceedings of the 35th International Conference on Machine Learning*. PMLR, Jul. 2018, pp. 2965–2974, iSSN: 2640-3498. [Online]. Available: <https://proceedings.mlr.press/v80/lehtinen18a.html>
- [7] J. Batson and L. Royer, "Noise2Self: Blind Denoising by Self-Supervision," in *Proceedings of the 36th International Conference on Machine Learning*. PMLR, May 2019, pp. 524–533, iSSN: 2640-3498. [Online]. Available: <https://proceedings.mlr.press/v97/batson19a.html>
- [8] A. Bora, E. Price, and A. G. Dimakis, "Ambientgan: Generative models from lossy measurements," in *International conference on learning representations*, 2018.
- [9] J. Tachella, D. Chen, and M. Davies, "Sensing Theorems for Unsupervised Learning in Linear Inverse Problems," *Journal of Machine Learning Research*, vol. 24, no. 39, pp. 1–45, 2023. [Online]. Available: <http://jmlr.org/papers/v24/22-0315.html>
- [10] D. Chen, J. Tachella, and M. E. Davies, "Equivariant Imaging: Learning Beyond the Range Space," in *2021 IEEE/CVF International Conference on Computer Vision (ICCV)*. Montreal, QC, Canada: IEEE, Oct. 2021, pp. 4359–4368. [Online]. Available: <https://ieeexplore.ieee.org/document/9711083/>
- [11] —, "Robust Equivariant Imaging: a fully unsupervised framework for learning to image from noisy and partial measurements," in *2022 IEEE/CVF Conference on Computer Vision and Pattern Recognition (CVPR)*. New Orleans, LA, USA: IEEE, Jun. 2022, pp. 5637–5646. [Online]. Available: <https://ieeexplore.ieee.org/document/9880116/>
- [12] Y. Quan, Z. Chen, H. Zheng, and H. Ji, "Learning Deep Non-blind Image Deconvolution Without Ground Truths," in *Computer Vision – ECCV 2022*, ser. Lecture Notes in Computer Science, S. Avidan, G. Brostow, M. Cissé, G. M. Farinella, and T. Hassner, Eds. Cham: Springer Nature Switzerland, 2022, pp. 642–659.
- [13] A. Shocher, N. Cohen, and M. Irani, "Zero-Shot Super-Resolution Using Deep Internal Learning," in *2018 IEEE/CVF Conference on Computer Vision and Pattern Recognition*. Salt Lake City, UT: IEEE, Jun. 2018, pp. 3118–3126. [Online]. Available: <https://ieeexplore.ieee.org/document/8578427/>
- [14] L. Xu, J. S. Ren, C. Liu, and J. Jia, "Deep Convolutional Neural Network for Image Deconvolution," in *Advances in Neural Information Processing Systems*, vol. 27. Curran Associates, Inc., 2014.
- [15] W. Ren, J. Zhang, L. Ma, J. Pan, X. Cao, W. Zuo, W. Liu, and M.-H. Yang, "Deep Non-Blind Deconvolution via Generalized Low-Rank Approximation," in *Advances in Neural Information Processing Systems*, vol. 31. Curran Associates, Inc., 2018.
- [16] J. Dong, S. Roth, and B. Schiele, "Deep Wiener Deconvolution: Wiener Meets Deep Learning for Image Deblurring," in *Advances in Neural Information Processing Systems*, vol. 33. Curran Associates, Inc., 2020, pp. 1048–1059.
- [17] J. Liang, J. Cao, G. Sun, K. Zhang, L. Van Gool, and R. Timofte, "SwinIR: Image Restoration Using Swin Transformer," in *2021 IEEE/CVF International Conference on Computer Vision Workshops (ICCVW)*. Montreal, BC, Canada: IEEE, Oct. 2021, pp. 1833–1844. [Online]. Available: <https://ieeexplore.ieee.org/document/9607618/>
- [18] C. Belthangady and L. A. Royer, "Applications, promises, and pitfalls of deep learning for fluorescence image reconstruction," *Nature methods*, vol. 16, no. 12, pp. 1215–1225, 2019.
- [19] U. S. Kamilov, C. A. Bouman, G. T. Buzzard, and B. Wohlberg, "Plug-and-play methods for integrating physical and learned models in computational imaging: Theory, algorithms, and applications," *IEEE Signal Processing Magazine*, vol. 40, no. 1, pp. 85–97, 2023.
- [20] D. Ulyanov, A. Vedaldi, and V. Lempitsky, "Deep image prior," in *Proceedings of the IEEE conference on computer vision and pattern recognition*, 2018, pp. 9446–9454.
- [21] D. Ren, K. Zhang, Q. Wang, Q. Hu, and W. Zuo, "Neural blind deconvolution using deep priors," in *Proceedings of the IEEE/CVF Conference on Computer Vision and Pattern Recognition*, 2020, pp. 3341–3350.
- [22] G. Mataev, P. Milanfar, and M. Elad, "Deepred: Deep image prior powered by red," in *Proceedings of the IEEE/CVF International Conference on Computer Vision Workshops*, 2019, pp. 0–0.
- [23] C. M. Stein, "Estimation of the Mean of a Multivariate Normal Distribution," *The Annals of Statistics*, vol. 9, no. 6, pp. 1135–

- 1151, 1981, publisher: Institute of Mathematical Statistics. [Online]. Available: <https://www.jstor.org/stable/2240405>
- [24] Y. C. Eldar, "Generalized SURE for Exponential Families: Applications to Regularization," *IEEE Transactions on Signal Processing*, vol. 57, no. 2, pp. 471–481, Feb. 2009, conference Name: IEEE Transactions on Signal Processing.
- [25] A. A. Hendriksen, D. M. Pelt, and K. J. Batenburg, "Noise2Inverse: Self-supervised deep convolutional denoising for tomography," *IEEE Transactions on Computational Imaging*, vol. 6, pp. 1320–1335, 2020, arXiv:2001.11801 [cs, eess, stat]. [Online]. Available: <http://arxiv.org/abs/2001.11801>
- [26] K. Fatania, K. Y. Chau, C. M. Pirkel, M. I. Menzel, and M. Golbabaei, "Nonlinear Equivariant Imaging: Learning Multi-Parametric Tissue Mapping without Ground Truth for Compressive Quantitative MRI," in *2023 IEEE 20th International Symposium on Biomedical Imaging (ISBI)*, Apr. 2023, pp. 1–4, iSSN: 1945-8452.
- [27] J. Tachella, D. Chen, and M. Davies, "Sensing Theorems for Unsupervised Learning in Linear Inverse Problems," *Journal of Machine Learning Research*, vol. 24, no. 39, pp. 1–45, 2023.
- [28] A. Bourrier, M. E. Davies, T. Peleg, P. Pérez, and R. Gribonval, "Fundamental Performance Limits for Ideal Decoders in High-Dimensional Linear Inverse Problems," *IEEE Transactions on Information Theory*, vol. 60, no. 12, pp. 7928–7946, Dec. 2014.
- [29] M. Vetterli, J. Kovačević, and V. K. Goyal, *Foundations of signal processing*. Cambridge University Press, 2014.
- [30] S. Ramani, T. Blu, and M. Unser, "Monte-carlo sure: A black-box optimization of regularization parameters for general denoising algorithms," *IEEE Transactions on image processing*, vol. 17, no. 9, pp. 1540–1554, 2008.
- [31] J.-B. Grill, F. Strub, F. Altché, C. Tallec, P. Richemond, E. Buchatskaya, C. Doersch, B. Avila Pires, Z. Guo, M. Gheshlaghi Azar *et al.*, "Bootstrap your own latent—a new approach to self-supervised learning," *Advances in neural information processing systems*, vol. 33, pp. 21 271–21 284, 2020.
- [32] X. Chen and K. He, "Exploring Simple Siamese Representation Learning," Nov. 2020, arXiv:2011.10566 [cs]. [Online]. Available: <http://arxiv.org/abs/2011.10566>
- [33] Y. Zhu, K. Zhang, J. Liang, J. Cao, B. Wen, R. Timofte, and L. Van Gool, "Denoising diffusion models for plug-and-play image restoration," in *Proceedings of the IEEE/CVF Conference on Computer Vision and Pattern Recognition*, 2023, pp. 1219–1229.
- [34] Y. C. Eldar, "Generalized sure for exponential families: Applications to regularization," *IEEE Transactions on Signal Processing*, vol. 57, no. 2, pp. 471–481, 2008.
- [35] K. Zhang, W. Zuo, S. Gu, and L. Zhang, "Learning deep cnn denoiser prior for image restoration," in *Proceedings of the IEEE conference on computer vision and pattern recognition*, 2017, pp. 3929–3938.
- [36] M. Z. Darestani and R. Heckel, "Accelerated mri with un-trained neural networks," *IEEE Transactions on Computational Imaging*, vol. 7, pp. 724–733, 2021.
- [37] E. Agustsson and R. Timofte, "NTIRE 2017 Challenge on Single Image Super-Resolution: Dataset and Study," in *2017 IEEE Conference on Computer Vision and Pattern Recognition Workshops (CVPRW)*. Honolulu, HI, USA: IEEE, Jul. 2017, pp. 1122–1131. [Online]. Available: <http://ieeexplore.ieee.org/document/8014884/>
- [38] J.-B. Huang, A. Singh, and N. Ahuja, "Single image super-resolution from transformed self-exemplars," in *2015 IEEE Conference on Computer Vision and Pattern Recognition (CVPR)*. Boston, MA, USA: IEEE, Jun. 2015, pp. 5197–5206.
- [39] S. G. Armato III, G. McLennan, L. Bidaut, M. F. McNitt-Gray, C. R. Meyer, A. P. Reeves, B. Zhao, D. R. Aberle, C. I. Henschke, E. A. Hoffman *et al.*, "The lung image database consortium (lidc) and image database resource initiative (idri): a completed reference database of lung nodules on ct scans," *Medical physics*, vol. 38, no. 2, pp. 915–931, 2011.
- [40] D. P. Kingma and J. Ba, "Adam: A method for stochastic optimization," *arXiv preprint arXiv:1412.6980*, 2014.
- [41] E. Quemener and M. Corvellec, "Sidus—the solution for extreme deduplication of an operating system," *Linux Journal*, vol. 2013, no. 235, p. 3, 2013.
- [42] K. Ma, Z. Duanmu, Q. Wu, Z. Wang, H. Yong, H. Li, and L. Zhang, "Waterloo exploration database: New challenges for image quality assessment models," *IEEE Transactions on Image Processing*, vol. 26, no. 2, pp. 1004–1016, 2016.
- [43] R. Timofte, E. Agustsson, L. Van Gool, M.-H. Yang, and L. Zhang, "Ntire 2017 challenge on single image super-resolution: Methods and

results," in *Proceedings of the IEEE conference on computer vision and pattern recognition workshops*, 2017, pp. 114–125.

## APPENDIX

We prove the two theorems introduced in Section III and define the Fourier transform and the convolution operation.

**Definition 3** (Fourier transform, inverse Fourier transform). *Let  $z \in \mathcal{S}$ , we consider the Fourier transform of  $z$  to be the function  $\hat{z} \in \mathcal{S}$  defined by*

$$\hat{z}(\xi) = \int_{\mathbb{R}^2} z(u) e^{-i2\pi\xi^\top u} du, \quad \xi \in \mathbb{R}^2. \quad (23)$$

*Conversely, for  $\hat{z} \in \mathcal{S}$ , the inverse Fourier transform of  $\hat{z}$  is the function  $z \in \mathcal{S}$  defined by*

$$z(u) = \int_{\mathbb{R}^2} \hat{z}(\xi) e^{i2\pi\xi^\top u} d\xi, \quad u \in \mathbb{R}^2. \quad (24)$$

**Definition 4** (Convolution). *Let  $h, z \in \mathcal{S}$ , we consider the convolution of  $h$  and  $z$  to be the function  $h * z \in \mathcal{S}$  defined by*

$$(h * z)(u) = \int_{\mathbb{R}^2} h(v) z(u - v) dv, \quad u \in \mathbb{R}^2. \quad (25)$$

**Theorem 1.** *Let  $h, \varphi \in \mathcal{S}$ . If  $h$  and  $\varphi$  are bandlimited with bandwidths  $\xi_h < \xi_\varphi$ , then there are sets  $\mathcal{Z}_1, \mathcal{Z}_2 \subseteq \mathcal{S}$  such that*

- $\mathcal{Z}_1$  and  $\mathcal{Z}_2$  are roto-translation invariant, that is

$$\tau_v R_\theta z \in \mathcal{Z}_\ell, \quad z \in \mathcal{Z}_\ell, v \in \mathbb{R}^2, \theta \in [0, 2\pi), \ell \in \{1, 2\}, \quad (9)$$

- for  $\mathcal{Y}_1 = h * \mathcal{Z}_1$  and  $\mathcal{Y}_2 = h * \mathcal{Z}_2$  as in Eq. (3),

$$\mathcal{Y}_1 = \mathcal{Y}_2 \quad (10)$$

- for  $\mathcal{X}_1 = \varphi * \mathcal{Z}_1$  and  $\mathcal{X}_2 = \varphi * \mathcal{Z}_2$  as in Eq. (4),

$$\mathcal{X}_1 \neq \mathcal{X}_2. \quad (11)$$

*Proof.* Let's assume that  $h$  and  $\varphi$  are bandlimited with  $\xi_h < \xi_\varphi$ . Let

$$\mathcal{Z}_1 = \{ z \in \mathcal{S}, \hat{z}(\xi) = 0, \forall \|\xi\|_2 \geq \xi_h \} \quad (26)$$

be the set of images with bandwidth at most  $\xi_h$  and  $\mathcal{Z}_2 = \mathcal{S}$  the set of all images (bandlimited or not). We show that 1)  $\mathcal{Z}_1$  and  $\mathcal{Z}_2$  are invariant under roto-translations, 2) that  $\mathcal{Y}_1 = \mathcal{Y}_2$ , and 3) that  $\mathcal{X}_1 \neq \mathcal{X}_2$ . 1) The subset  $\mathcal{Z}_2$  is the whole image space  $\mathcal{S}$  which is invariant under roto-translations, and since the bandwidth of an image does not change under roto-translations, the subset  $\mathcal{Z}_1$  is also invariant under roto-translations. 2) The subsets  $\mathcal{Z}_1$  and  $\mathcal{Z}_2$  contain every image with bandwidth at most  $\xi_h$  so  $\mathcal{Y}_1$  and  $\mathcal{Y}_2$  are both equal to the set of all images with bandwidth at most  $\xi_h$  which also vanish when the filter vanishes

$$\mathcal{Y}_1 = \mathcal{Y}_2 = \{ y \in \mathcal{S}, \hat{h}(\xi) = 0 \implies \hat{y}(\xi) = 0, \forall \xi \in \mathbb{R}^2 \}. \quad (27)$$

3) Consider the image  $x = \varphi * \varphi$ , it has bandwidth  $\xi_\varphi$  and it is of the form  $\varphi * z$  for  $z \in \mathcal{S}$ , so  $x \in \mathcal{X}_2$  but  $x \notin \mathcal{X}_1$  as  $\mathcal{X}_1$  contains only images with bandwidth at most  $\xi_h$  and  $\xi_h < \xi_\varphi$ .  $\square$

**Theorem 2.** Let  $h, \varphi \in \mathcal{S}$  and  $\mathcal{Z} \subseteq \mathcal{S}$ . If  $\mathcal{Z}$  is scale-invariant, that is

$$\Sigma_s z \in \mathcal{Z}, \forall z \in \mathcal{Z}, s \in (0, \infty), \quad (12)$$

$\varphi$  is bandlimited, and  $\hat{h}(0) \neq 0$ , where  $\hat{h}$  is the Fourier transform of  $h$ , then the set  $\mathcal{X}$  defined in Eq. (4) is uniquely determined by the set of observed images  $\mathcal{Y}$  defined in Eq. (3). More precisely, there is a  $s \geq \frac{\xi_\varphi}{\xi_h}$  which only depends on  $\varphi$  and  $h$ , for which  $\hat{h}(s^{-1}\xi) \neq 0$  as long as  $\|\xi\|_2 < \xi_\varphi$ , and

$$\mathcal{X} = \{x_y, y \in \mathcal{Y}\}, \quad (13)$$

where  $x_y \in \mathcal{S}$  is defined by

$$\hat{x}_y(\xi) = \begin{cases} \frac{\hat{\varphi}(\xi)\hat{y}(s^{-1}\xi)}{s\hat{h}(s^{-1}\xi)}, & \text{if } \|\xi\|_2 < \xi_\varphi, \\ 0, & \text{otherwise.} \end{cases} \quad (14)$$

*Proof.* Let  $\xi \in \mathbb{R}^2$ . Since  $\hat{h}(0) \neq 0$ , and since  $\hat{h}$  is continuous as it is in  $\mathcal{S}$ , there is a  $\xi_h > R_h > 0$  such that

$$\hat{h}(\xi) \neq 0, \forall \xi \in \mathbb{R}^2, \|\xi\|_2 \leq R_h. \quad (28)$$

Let  $s = \frac{\xi_\varphi}{R_h}$  and

$$\hat{\mathcal{X}} = \{x_y, y \in \mathcal{Y}\}. \quad (29)$$

Notice that  $x_y$  as defined in Eq. (14) is only well-defined if  $\hat{h}(s^{-1}\xi) \neq 0$  for all  $\|\xi\|_2 < \xi_\varphi$ , or equivalently if  $\hat{h}(\xi) \neq 0$  for all  $\|\xi\| < s^{-1}\xi_\varphi = R_h$ , which is the case for that specific value of  $s$ . We are going to show that  $\hat{\mathcal{X}} = \mathcal{X}$  where

$$\mathcal{X} = \{\varphi * z, z \in \mathcal{Z}\}. \quad (30)$$

First, we show that  $\hat{\mathcal{X}} \subseteq \mathcal{X}$ . For  $y \in \mathcal{Y}$ , there is a  $z \in \mathcal{Z}$  such that

$$y = h * z, \quad (31)$$

and according to the convolution theorem,

$$\hat{y}(s^{-1}\xi) = h(s^{-1}\xi)\hat{z}(s^{-1}\xi). \quad (32)$$

The  $\hat{x}_y$  associated with this  $y$  is obtained by replacing Eq. (32) in Eq. (14)

$$\hat{x}_y(\xi) = \begin{cases} s^{-1}\hat{\varphi}(\xi)\hat{z}(s^{-1}\xi), & \text{if } \|\xi\|_2 < \xi_\varphi, \\ 0, & \text{otherwise.} \end{cases} \quad (33)$$

Now, let  $z_s = \Sigma_{s^{-1}}z$ , according to the scaling formula for the Fourier transform,

$$\hat{z}_s(\xi) = s^{-1}\hat{z}(s^{-1}\xi). \quad (34)$$

Since  $z \in \mathcal{Z}$  and since  $\mathcal{Z}$  is invariant to scale,  $z_s \in \mathcal{Z}$  and  $x \in \mathcal{X}$  for

$$x = \varphi * z_s. \quad (35)$$

Moreover, according to the convolution theorem,

$$\hat{x}(\xi) = \hat{\varphi}(\xi)\hat{z}_s(\xi), \quad (36)$$

and more precisely since  $\varphi$  is bandlimited

$$\hat{x}(\xi) = \begin{cases} \hat{\varphi}(\xi)\hat{z}_s(\xi), & \text{if } \|\xi\|_2 < \xi_\varphi, \\ 0, & \text{otherwise.} \end{cases} \quad (37)$$

Comparing Eq. (33) with Eq. (37) we have

$$\hat{x}_y(\xi) = \hat{x}(\xi), \quad (38)$$

thus  $x_y = x$ , and since  $x \in \mathcal{X}$ ,  $\hat{\mathcal{X}} \subseteq \mathcal{X}$ .

Conversely, we show that  $\mathcal{X} \subseteq \hat{\mathcal{X}}$ . Let  $x \in \mathcal{X}$ , then there is a  $z \in \mathcal{Z}$  such that

$$x = \varphi * z. \quad (39)$$

Now, let

$$y_s = h * (\Sigma_s z). \quad (40)$$

According to the convolution theorem,

$$\hat{x}(\xi) = \hat{\varphi}(\xi)\hat{z}(\xi), \quad (41)$$

and

$$\hat{y}_s(\xi) = \hat{h}(\xi)\hat{z}_s(\xi), \quad (42)$$

where  $z_s = \Sigma_s z$ , and according to the scaling formula for the Fourier transform,

$$\hat{z}_s(\xi) = s\hat{z}(s\xi) = s(\Sigma_{s^{-1}}\hat{z})(\xi), \quad (43)$$

as

$$z_s(u) = z(s^{-1}u), \forall u \in \mathbb{R}^2. \quad (44)$$

If  $\|\xi\|_2 < \xi_\varphi$ , then it follows directly from the previous equations that

$$\hat{x}(\xi) = \hat{\varphi}(\xi)\hat{z}(\xi), \quad (45)$$

$$= \hat{h}(s^{-1}\xi)^{-1}\hat{\varphi}(\xi)\hat{h}(s^{-1}\xi)\hat{z}(\xi), \quad (46)$$

$$= \hat{h}(s^{-1}\xi)^{-1}\hat{\varphi}(\xi)\left(\hat{h}(s^{-1}\xi)\hat{z}(s s^{-1}\xi)\right), \quad (47)$$

$$= \hat{h}(s^{-1}\xi)^{-1}\hat{\varphi}(\xi)\left(\hat{h}(s^{-1}\xi)(\Sigma_{s^{-1}}\hat{z})(s^{-1}\xi)\right), \quad (48)$$

$$= \hat{h}(s^{-1}\xi)^{-1}\hat{\varphi}(\xi)\left(\hat{h}(s^{-1}\xi)(s^{-1}s\Sigma_{s^{-1}}\hat{z})(s^{-1}\xi)\right), \quad (49)$$

$$= s^{-1}\hat{h}(s^{-1}\xi)^{-1}\hat{\varphi}(\xi)\left(\hat{h}(s^{-1}\xi)\hat{z}_s(s^{-1}\xi)\right), \quad (50)$$

$$= s^{-1}\hat{h}(s^{-1}\xi)^{-1}\hat{\varphi}(\xi)\hat{y}_s(s^{-1}\xi). \quad (51)$$

Hence, as  $\varphi$  is bandlimited,

$$\hat{x}(\xi) = \begin{cases} \frac{\hat{\varphi}(\xi)\hat{y}_s(s^{-1}\xi)}{s\hat{h}(s^{-1}\xi)} & \text{if } \|\xi\|_2 < \xi_\varphi, \\ 0 & \text{otherwise,} \end{cases} \quad (52)$$

thus  $x = x_y$  and since  $y \in \mathcal{Y}$ ,  $x \in \hat{\mathcal{X}}$ , thus  $\mathcal{X} \subseteq \hat{\mathcal{X}}$ .  $\square$